TITAN
CARBON SEQUESTRATION

Underground Injection Control – Class VI Permit Application for Cronos No. 1 and Rhea No. 1

Jefferson County, Texas

SECTION 2 – PLUME MODEL

February 2024

LONQUIST SEQUESTRATION LLC

SECTION 2 – PLUME MODEL

TABLE OF CONTENTS

Figures

Tables

2.1 Introduction

The following discussion of the plume model used for Cronos No. 1 and Rhea No. 1, the proposed injection wells of the Titan Carbon Sequestration Project (Titan Project), was prepared to meet the requirements of Title 16, Texas Administrative Code (16 TAC) §5.**203(d)** [Title 40, U.S. Code of Federal Regulations (40 CFR) **§146.84**]. This section describes the key details of the reservoir model. The plume defines the pore space rights, area of review (AOR) for the well, monitoring plans, corrective action plan as necessary, and overall viability of the project. Both *Section 3 – AOR and Corrective Action Plan* and *Section 5 – Testing and Monitoring Plan* use the forecasted plume to help determine the best strategies and plans to minimize the impact of carbon sequestration.

The primary objectives of the plume model are to do the following:

1. Select the strategically best well locations for CO_2 storage.
2. Optimize the available pore space for supercritical CO_2 storage.
3. Minimize the impact of offset injection through completion-strategy implementation and well design.
4. Assess CO_2 migration and pressure increase to avoid adverse impact on major subsurface structures.

2.2 Project Summary

The Titan Project, located in Jefferson County, Texas, will be developed by Titan Carbon Sequestration, LLC (Titan), through underground storage easements. [redacted] Two injection wells are currently planned for the Titan Project, Cronos No. 1 and Rhea No. 1, located in the western portion of the easement area. The plume modeling is specific to these proposed injection wells. The two injection wells were included in the reservoir model to capture their interaction with each other. Each well injects [redacted] million metric tons annually (MMT/yr). Cronos No. 1 and Rhea No. 1 are planned to inject for [redacted] years concurrently, resulting in [redacted] million metric tons (MMT) of supercritical CO_2 being safely sequestered. Figure A-4 in *Appendix A* provides a detailed description of the property.

2.2.1 Software

2.2.1.1 Petrel™ Software Suite

Schlumberger's Petrel software was chosen to create a detailed geocellular model for the CCS site. This state-of-the-art software is used worldwide and combines information from logs and seismic data to build an accurate representation of the underground reservoir. The Petrel-developed geocellular model shows the different layers of the site, including the *Amphistegina B* (Amph B) (upper seal), Lower Miocene Sands (injection zone), and *Siphonina davisi* (Siph Dav) (lower seal). Using Petrel, the permeability and porosity properties of the injection zone were distributed, considering well-log analysis and established methods. These methodologies ensure a representative depiction of the reservoir in the model.

2.2.1.2 Computer Modelling Group's Software Suite

The geocellular model was developed in Petrel and then input into CMG's GEM 2023.20 (GEM) simulator, a widely recognized tool for modeling compositional fluid flow in conventional and unconventional reservoirs. The simulator uses advanced computational methods and equation-of-state (EOS) algorithms to evaluate compositional and chemical processes to produce a reliable CCS simulation. The software can handle large data sets and multiple grids, and offers various tools for data management, visualization, and uncertainty analysis.

2.2.2 Data Sources

Constructing the geocellular and dynamic model involved the use of 3D seismic data, offset well logs, core data, and publicly available literature, such as peer-reviewed papers of the Society of Petroleum Engineers (SPE) and the American Association of Petroleum Geologists (AAPG).

A comprehensive review of public databases and literature was carried out at both regional and site-specific levels. At the regional level, major trends within the project area and its surroundings were identified. These trends were then compared to more site-specific data to increase confidence in the reservoir properties. Using nearby offset well data, trends in reservoir salinity and temperature were estimated. Additionally, regional data pointed towards analogous reservoirs to incorporate into the model. Key properties like rock compressibility and relative permeability were gathered from the publicly available literature. These assumptions are further discussed in *Section 2.5.2*.

Offset log analysis was conducted to further characterize the reservoir and populate the geocellular model. Openhole log data included various analyses such as gamma ray, spontaneous potential, resistivity, porosity (sonic, neutron, density), photoelectric factor, caliper, and other related analyses. These well logs helped determine formation tops, rock properties, and temperature gradients. Petrophysical analysis was performed on six wells in the Titan Project vicinity to assess the target injection zone and subsequent confining zones.

To enhance the characterization of the reservoir, 3D seismic data was used in conjunction with formation tops identified through log analysis—to identify major structural horizons as shown in Figure 2-1. The 3D seismic data also offered improved clarity of the subsurface, aiding in the identification of major structural horizons, as well as any structural alterations like faults, salt domes, or other subsurface changes. This data enhanced the accuracy of the geocellular model by providing a clearer understanding of the targeted stratigraphy.

[redacted]

Figure 2-1 – Major stratigraphic units in the geologic model displayed in southwest-northeast section.

Analogous core data was used to determine the porosity-permeability relationship in the Lower Miocene. The core data comes from the [redacted] [redacted] of the injection site. Site-specific data will be collected after submittal of this permit application. A stratigraphic test well is planned to gather core, fluid samples, and geophysical logs. The inclusion of the additional data will further increase the accuracy of the model and simulation results.

2.3 Trapping Mechanisms

In the context of a CCS project, four mechanisms are key for trapping and storing supercritical CO_2, as illustrated in Figure 2-2. The following sections will cover structural and stratigraphic trapping, residual trapping, solubility trapping, and mineral trapping mechanisms. All mechanisms except for mineral trapping are present in the current model.

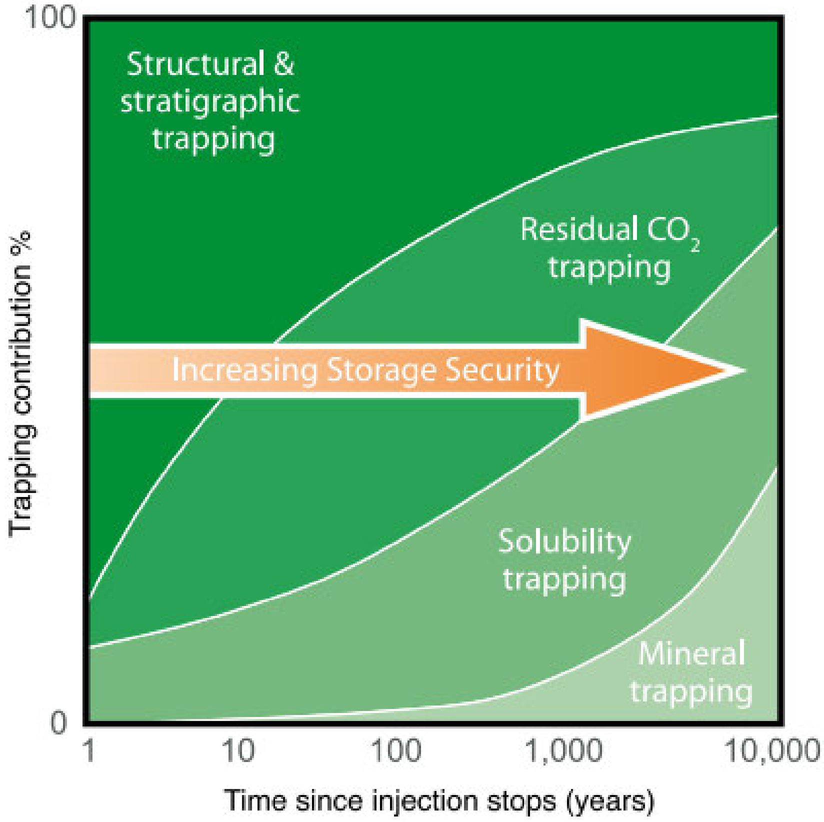

Figure 2-2 – CO_2 Storage Mechanisms (Metz et al., 2005)

2.3.1 Structural and Stratigraphic Trapping

Structural and stratigraphic trapping involves the physical immobilization of injected supercritical CO_2 through the presence of geological features like sealing faults, pinchouts, or other forms of geologic traps. Like naturally occurring hydrocarbon reservoirs, CO_2 can commonly be stored in anticlinal folds. Structural and stratigraphic trapping play a key role in trapping the injected supercritical CO_2 during and in the initial period after injection, but overtime is overtaken by more permanent trapping mechanisms. In this project specifically, the CO_2 is structurally trapped by the confining zone and thick interbedded shales. These features prevent any further vertical migration of the injected CO_2. Supercritical CO_2 is a low-viscosity fluid, less dense than the surrounding brine found in the injection zone. The CO_2 will continue to rise until its buoyant forces are no longer greater than the capillary entry pressure of the confining zone. For this model, the CO_2 mass density ranges [redacted] The surrounding brine density is [redacted]

To determine the CO_2 phase and associated properties, EOS calculations are performed using formulas that can predict the density of the injected fluid at any location based on pressure and temperature. The GEM uses several well-known EOS formulas, including the Van der Waals equation, the Peng-Robinson method, and the Soave-Redlich-Kwong (SRK) method. The EOS implemented within the plume model was the Peng-Robinson method, due to its widely accepted use for volumetric and phase equilibria.

2.3.2 Residual Trapping

Residual trapping is a physical form of trapping where discontinuous CO_2 is left behind and becomes trapped in the pore space as the plume continues to migrate. As water is displaced in the rock, the CO_2 fills the space. However, depending on the movement of CO_2 and the aqueous phase through saturation and capillary forces, CO_2 will remain residually trapped within the pore space. Within the Miocene sandstone environment, larger quantities of sand are available for the CO_2 to migrate to and become residually trapped. Laboratory testing shows that residual trapping of CO_2 accounts for the majority of the overall trapping within high permeability sandstones during the proposed monitoring period (Burnside and Naylor, 2014). Based on dynamic plume modeling, residual trapping is the main trapping mechanism during the proposed monitoring period (Figure 2-37).

To accurately predict the amount of supercritical CO_2 that remains residually trapped, the model employs hysteresis modeling. The GEM software offers several methods to determine residual trapping, such as the Carlson and Land model and the Larsen and Skauge model. The Carlson and Land model was implemented for this simulation due to (1) its use being validated for water-alternating-gas (WAG) injection and (2) its ability to model a two-phase system. The critical parameter—residual (trapped) gas saturation—will be discussed in *Section 2.5.3*.

2.3.3 Solubility Trapping

Solubility trapping is a form of chemical trapping between the injected supercritical CO_2 and surrounding formation brine. In brine, CO_2 is highly soluble, resulting in a solution that has a higher density than the connate brine. This action causes the higher density brine to sink within the formation and traps the CO_2-entrained brine. This dissolution allows for an increased storage capacity and decreased fluid migration. The salinity, pressure, and temperature of the surrounding brine all affect the solubility of CO_2 and the rate at which the dissolution occurs. While solubility trapping takes place in the dynamic plume model, this trapping mechanism can take hundreds to thousands of years to overtake residual trapping as the main mechanism for trapping CO_2 (Figure 2-2). During the project's proposed monitoring period, solubility trapping is second to residual trapping as the main trapping mechanism, based on the dynamic plume model (Figure 2-37).

For solubility modeling, GEM offers the options of the Harvey and Li-Ngheim methods. The Li-Ngheim method was chosen due to its accuracy in modeling CO_2 solubility at high salinities. This method also incorporates solubility parameters specific to CO_2, as defined by the constant correlations of Henry's law.

2.3.4 Mineral Trapping

Mineral or geochemical trapping is another form of chemical trapping that occurs due to reactions between CO_2 and the geochemistry of the formation. During injection of CO_2 into the reservoir, four primary drivers interact with each other: (1) CO_2 in supercritical phase, (2) in situ hydrochemistry of the connate brine, (3) aqueous CO_2, and (4) the geochemistry of the formation rock. The interaction of these components results in CO_2 often being precipitated out as a newly formed mineral—typically Ca-CO_3, or calcium carbonate (i.e., limestone).

Mineral trapping can also occur due to the adsorption of CO_2 onto clay minerals. Once hysteresis and solubility trapping are included in the model, geochemical formulas can be added through an internal geochemistry database to describe mineral-trapping reactions. For aqueous reactions, the following formulas were used:

$$CO_2(aq) + H_2O = H^+ + HCO_3^-$$
$$CO_3^{-2} + H^+ = HCO_3^-$$
$$OH^- + H^+ = H_2O$$

These three reactions are common ionic reactions that can occur in the reservoir between water and CO_2. The following formulas show the mineral reactions used within the model. Each mineral is commonly found within sandstone in an underground aquifer and causes the precipitation of carbon oxides in a solid state:

$$Anthorite\ (CaAl_2Si_2O_8) + 8H^+ = 4H_2O + Ca^{2+} + 2Al^{2+}$$
$$Calcite\ (CaCO_3) + H^+ = Ca^{2+} + HCO_3^-$$
$$Kaolinite\ (Al_2Si_2O_5(OH_4)) + 6H^+ = 5H_2O + 2Al^{3+} + 2SiO$$

While geochemical trapping can have a greater impact on CO_2 over hundreds or thousands of years, the short-term effects of these trapping mechanisms are small, and fluid movement is predominated by hydrodynamic and solubility trapping. Due to the current limitations in data for the compositions of these minerals and components in the reservoir, as well as the computational stress added to the software, the geochemical trapping mechanisms were not assumed in the current model. As more data are received on the geochemical properties of the reservoir, sensitivities could be run to determine the relative importance of this trapping mechanism over time.

2.4 Conceptual Site Model

2.4.1 Geologic Model Development

Using Petrel, the model incorporated [redacted] to define the structural framework. A horizontal cell dimension of [redacted] t was applied. [redacted]

[redacted]. Lithofacies were then interpreted from the well logs and scaled up to the 3D grid-cell dimensions. Next, the data was analyzed using seismic attributes and geostatistics to help define the vertical and lateral continuity and orientation of the facies. These results were used to populate the facies well control throughout the 3D model, using the sequential indicator simulation algorithm. The generated facies model was then used to condition the distribution of the porosity, resulting in the porosity model. The geocellular model is referenced to the North American Datum of 1927 (NAD 27) and was projected into the Texas State Plane before being exported to GEM.

The sources of data incorporated into the geocellular model were seismic surveys and well data, such as locations, elevations, deviation, well tops, and well logs. Seismic surveys and well logs were used for interpretation and for the depth-conversion process.

2.4.2 Structural Framework

The geocellular model covers an area of [redacted] square miles (sq mi) as represented by the black polygon in Figure 2-3. A 3D seismic survey exists within the model area that covers [redacted] sq mi of that area, as represented by the red polygon. The outline for the Titan acreage is displayed in blue. The structural model was built on [redacted] (Figure 2-4).

[redacted]

Figure 2-3 – Map of the project area showing the Titan acreage outline (indicated in blue) and the 3D geomodel outline (in black).

[redacted]

Figure 2-4 – Structural model displayed in a 3D view as seen from a southwest perspective.

Figures 2-5 and 2-6 illustrate [redacted] the tops of the upper and lower confining surfaces, Amphistegina B (Amph B) and Siphonina Davisi (Siph Dav), respectively. [redacted]

[redacted]

Figure 2-5 – Structural Map for the Top of Amph B – Top of the Upper Confinement Zone [redacted]

[redacted]

Figure 2-6 – Structural Map for the Top of Siph Dav – Top Lower Confining Zone [redacted]

2.4.3 Rock Property Distribution

2.4.3.1 Lithofacies Distribution

Lithofacies were interpreted for [redacted] wells with spontaneous potential (SP) or gamma ray (GR) logs. Figure 2-7 displays the northwest-to-southeast well section showing the SP/GR logs and interpreted facies. The reference map is provided in Figure 2-8 (page 15). If an SP log was not available, a GR one was used. A shale baseline was selected for each SP or GR log based on log character for individual wells. This baseline was used to separate the sand from the shale. The cutoff values varied since they were chosen according to the shale baseline determined for each well. The interpreted facies logs based on the results obtained were then upscaled into the 3D grid and distributed to create a facies model using geostatistics.

[redacted]

Figure 2-7 – Northwest-southeast well section displaying SP logs and interpreted lithofacies results (map location shown in Figures 2-8 and 2-10).

[redacted]

Figure 2-8 – Base map displaying northwest-southeast well section (from Figures 2-7 and 2-10).
The wells were used for the lithofacies interpretation. The Cronos No. 1 and Rhea No. 1 injection wells are displayed in black.

The geostatistical analysis included the generation of vertical, major, and minor variograms from upscaled facies logs derived from the defined SP/GR cutoffs. The variograms were calculated for each one of the zones in the model. An example of a typical variogram from this study is shown in Figure 2-9, displaying the vertical, major, and minor variograms for the Lower Miocene sands. The anisotropy observed has [redacted] This [redacted] trend is also observed in the seismic attributes and the other injection interval, as shown in Figure 2-10. The K Slice from this figure is from the injection zone and overlies the Marg Asc. Table 2-1 displays the variogram ranges and target-facies fractions for each of the sand intervals in the project. The target-facies fractions are derived from the upscaled-facies log.

[redacted]

Figure 2-9 – Typical vertical and horizontal variograms, calculated in this study for the Lower Miocene – Rob L interval.

[redacted]

Figure 2-10 – K layer 293 from the injector zone (just above Marg Asc) through the model displaying seismic amplitude sampled to the cells in the model. [redacted]

Table 2-1 – Facies Variograms and Target Percentages from Well Logs

Zone	Vertical Range (ft)	Major Range (ft)	Minor Range (ft)	Facies Fraction
Amph B – Lower Mio	[redacted]	[redacted]	[redacted]	[redacted]
Lower Mio – Rob L	[redacted]	[redacted]	[redacted]	[redacted]
Rob L – Siph Dav	[redacted]	[redacted]	[redacted]	[redacted]

The sequential indicator simulation algorithm was used to populate the facies distribution, using the variograms and target-facies fractions listed in Table 2-1. The vertical-facies proportions from the upscaled log were also used to capture the vertical trends.

The facies model is observed in Figure 2-11, and a southwest-to-northeast cross section through the model is shown in Figure 2-12. Sand lithofacies are represented in yellow and shale in gray.

[redacted]

Figure 2-11 – Facies model in a 3D window. The location of the cross section from Figure 2-12 is represented by the gray plane.

[redacted]

Figure 2-12 – Southwest-to-northeast cross section through the facies model shown in Figure 2-11. Perforation stages are displayed in the injector wells.

2.4.3.2 Permeability/Porosity Distribution

A porosity model was also generated using [redacted] porosity log curves that were upscaled to the 3D grid. The values were distributed using the sequential Gaussian simulation algorithm and conditioned to the facies model already created. Figure 2-13 shows the location for the wells with porosity logs, while Figure 2-14 shows a southwest-northeast section through the porosity model and injector locations. The results of the porosity-distribution histogram are shown in Figure 2-15 (page 23).

[redacted]

Figure 2-13 – Base map showing the location of the [redacted] wells with porosity logs included in the distribution of the porosity model.

[redacted]

Figure 2-14 – Southwest-northeast section through the porosity model. The location of the section is represented by the polygon in Figure 2-13.

[redacted]

Figure 2-15 – Histogram comparing porosity from raw logs, upscaled cells, and porosity property model.

A porosity-permeability relationship was derived from offset core samples of one nearby well, the [redacted] Using these samples, a relationship was identified as displayed in Figure 2-16. This relationship was then applied to the porosity model to determine the permeability of the Lower Miocene sands. *Section 1.5.1* provides a more detailed explanation of this relationship.

[redacted]

Figure 2-16 – Porosity-Permeability Relationship Implemented Into the Geocellular Model

A regression equation was derived from Figure 2-16 and used to calculate the permeability property depicted in Equation 1:

(Eq. 1) $K(mD) =$ [redacted]

Where:
K(mD) is the resulting permeability model.
Φ_{eff} *is the porosity property discussed above, converted to percentage instead of fractions.*

All properties, facies, porosity, and permeability were exported to GEM for simulation.

2.5 Dynamic Plume Model

2.5.1 Model Orientation and Gridding Parameters

Spatial Conditions

As discussed in *Section 2.2.1.2*, CMG uses as an input the Petrel geocellular model, which encompasses approximately [redacted] The geocellular model is built in Petrel to capture available well control and seismic data in and around the Titan Project boundary. By incorporating information from well logs and seismic data encompassing an area larger than the project boundary, the geologic characterization of the reservoir is enhanced. Once the geocellular model is imported into CMG for dynamic modeling purposes, the large grid size allows for the pressure and plume extents to be fully captured and not constrained by the lateral extent of the grid. At its greatest extent, the grid extends [redacted] Figure 2-17 shows the porosity and permeability in the west-east cross-sectional view at Rhea No. 1, as it was imported from Petrel pre-cutoffs.

[redacted]

Figure 2-17 – Model Pre-cutoff at Rhea No. 1, West-East Cross-Sectional View

[redacted]

[redacted]

[redacted]

[redacted]

Figure 2-18 – Model Resizing for Improved Efficiency at Rhea No. 1, West-East Cross-Sectional view

Multiple distinct sand packages are identified as potential targets for supercritical CO_2 injection. Each package is separated by interbedded shales and shale baffles that may act as barriers that impede CO_2 movement. [redacted] To represent the sand packages more accurately between large gaps of well data and further validate the geocellular model, 3D seismic was used.

<u>Boundary Conditions</u>

The Miocene sands in the Gulf Coast exhibit extensive connectivity across the entire area. [redacted]

[redacted]

Figure 2-19 – [redacted]

Model Time Frame

[redacted] This duration allows for a comprehensive demonstration of plume stabilization. Details of the model's results are discussed in *Section 2.7.*

2.5.2 Initial Conditions

The geocellular model served as an input for constructing the dynamic plume model. The assumptions in Table 2-2 were also used to initialize the model. Porosity is geostatistically distributed and exported from Petrel, with values ranging from [redacted] in the injection zone. Applying the porosity-permeability relationship derived from petrophysical analysis for offset cores, the permeability ranges from [redacted] The pore and fracture pressure gradients were calculated to be [redacted], respectively. A regional and well log review estimated the temperature gradient to be [redacted] Salinity within the injection zone was determined to be approximately [redacted] as discussed in the brine salinity subsection (*Section 2.5.2.4*).

Table 2-2 – Initial-Conditions Inputs Summary

Inputs	Values
Average Porosity (%)	[redacted]
Average Permeability (mD)	[redacted]
Average Kv/Kh Ratio	[redacted]
Pore Pressure Gradient (psi/ft)	[redacted]
Frac Pressure Gradient (psi/ft)	[redacted]
Mean Surface Temperature (°F)	[redacted]
Temperature Gradient (°F/100 ft)	[redacted]
Salinity (ppm)	[redacted]

[redacted]

2.5.2.1 Porosity/Permeability

As discussed in *Section 2.4*, porosity is determined through the analysis of openhole logs, and permeability is calculated using a porosity-permeability relationship (Figure 2-16, *Section 2.4.3.2*), derived from core data taken from a nearby offset well within the Lower Miocene. The permeability relationship implemented in the dynamic model is depicted in Equation 1 in *Section 2.4.3.2*.

Porosity is geostatistically distributed throughout the model. The porosity-permeability equation is then applied to all sand facies grid cells to determine reservoir permeability. This process results in a porosity range of [redacted] and a permeability range of [redacted] in all sands. Shales are expected to be clay-rich in this depositional environment. Clay-rich shales show permeability values in the range of 0.1 nano-darcy to 100 nano-darcy (Backeberg et al., 2017). In the dynamic model, a permeability value of [redacted] is assumed for the shale facies. These distributions are shown west to east in Figure 2-18 (*Section 2.5.1*).

The vertical permeability [redacted]

2.5.2.2 Pressure Gradient

The reservoir simulation model for Cronos No. 1 and Rhea No. 1 assumes a reservoir filled with 100% brine. The formation is assumed to be in hydrostatic conditions. Pore pressure for the injection zone was estimated from log data of the [redacted] A total dissolved solids (TDS) curve was prepared using resistivity data. The TDS values were used to calculate fluid density and pore pressure, using McCain's Correlation (McCain, 1991) in half-foot intervals. The resulting pore pressure vs. depth curve is included in Figure 2-20, and the equation used to calculate the pore pressure gradient is given in Equation 2. The pressure gradient used in this model is [redacted] psi/ft, which correlates to the calculated density. This value is used to help initialize GEM's reservoir model to internally calculate the fluid density across the entire modeled area.

$$\text{(Eq. 2)} \qquad PPG\left(\frac{psi}{ft}\right) = 0.433 \cdot \left(1 + TDS_{Inj\,Zone} \cdot 10^{-6}\right)$$

Where:

PPG is the resulting pore pressure gradient in psi/ft.

0.433 is the pressure gradient of freshwater in psi/ft.

$TDS_{Inj\,Zone}$ is the total dissolved solids in the injection zone in ppm.

[redacted]

Figure 2-20 – Plot of pore pressure gradient vs. depth calculated from log data at the [redacted]

2.5.2.3 Fracture Gradient

Eaton's method (Eaton, 1969), widely acknowledged as the standard practice for the determination of fracture gradients, was used to calculate the pressure required to fracture the injectable rock. The method requires Poisson's ratio (v), overburden gradient (OBG), and pore gradient (PG) to be [redacted] psi/ft, to determine the fracture gradient. Table 2-3 provides the values of each input.

Table 2-3 – Fracture Gradient Calculation Assumptions – Eaton's Method

Inputs	Values
Poisson's Ratio	[redacted]
Overburden Gradient (psi/ft)	[redacted]
Pore Gradient (psi/ft)	[redacted]

Poisson's ratio was determined through an extensive literature review on unconsolidated sandstones and core data. Literature suggests that sandstones can have a wide range of potential Poisson's ratios (0.1–0.4). The review primarily focused on sandstones that closely resemble the unconsolidated nature of the Miocene sands. In 2014, a case study was done to model fracture initiation in poorly consolidated sandstone, resulting in a ratio of 0.27 (Sun et al., 2015). Further research showed that soft sandstones can have a range of 0.2–0.35 (Molina, Vilarras, and Zeidouni, 2017). [redacted]

With the inputs, it is possible to calculate a fracture gradient (FG). Equation 3 highlights the necessary steps for calculating the gradient. Per TAC **§5.203(f)(2)(C)** [40 CFR **§146.88(a)**], the well may not exceed 90% of the FG during injection operations. Therefore, the model applied a pressure constraint of [redacted] psi/ft to all injectors.

(Eq. 3) $$FG = \frac{\nu}{1-\nu}(OBG - PG) + PG$$

[redacted]

2.5.2.4 Reservoir Fluid Properties

Reservoir Temperature

An evaluation of well logs near the Titan Project was conducted to estimate the reservoir temperature. From this evaluation, the nearest well log was chosen to provide the most analogous data point to the target formation. [redacted] This gradient is added onto a surface temperature of 70°F, the mean annual surface temperature.

Brine Salinity

A constant salinity value of [redacted] TDS was input into the model. This value is based on the average salinity estimates of the injection zone taken from well log analysis of the [redacted] This method of estimating salinity entails determining an apparent water resistivity (R_{wa}) by applying Archie's equation to porosity and resistivity data. Subsequently, the R_{wa} value is transformed into salinity using conventional petrophysical charts, provided by service companies such as SLB (previously known as Schlumberger).

2.5.3 Rock Properties Hysteresis Modeling

Rock (Pore Space Volume) Compressibility

A literature review was conducted to determine the rock compressibility of the Gulf Coast Miocene sands. Due to the lack of regional rock compressibility data, an expanded search for data into poorly sorted, unconsolidated sandstones was undertaken. The literature review analysis indicates that this type of formation can have compressibility values within a range of 10–40 microsips, as highlighted in Figure 2-21. [redacted] This assumption is subject to revision as additional data from the stratigraphic test well becomes available.

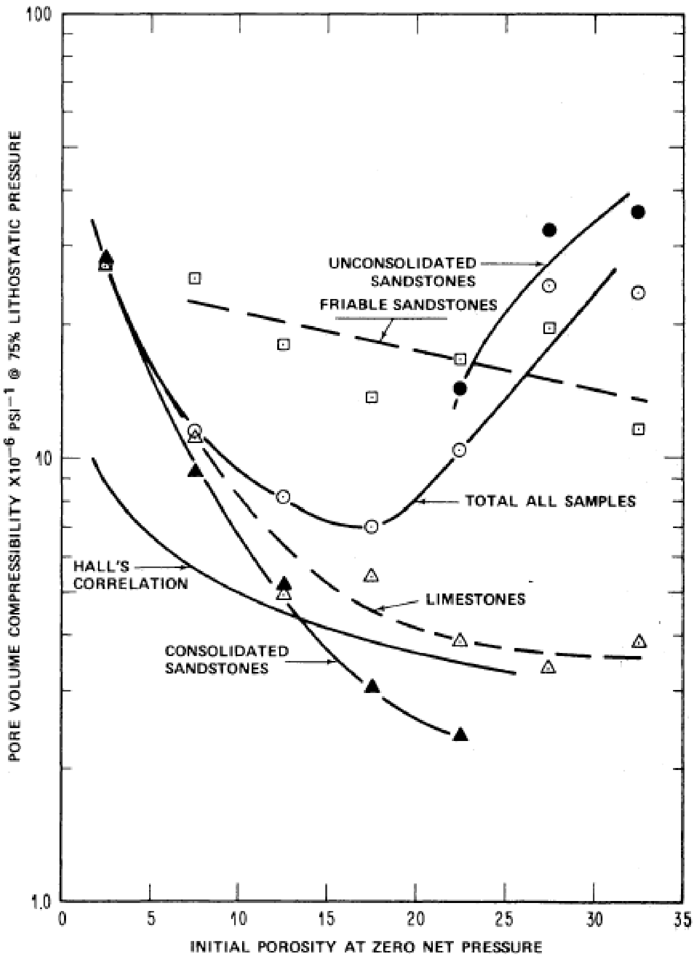

Figure 2-21 – Pore-Volume Compressibility vs. Initial Sample Porosity (Newman, 1973)

Residual Gas (Nonwetting Phase) Saturation

A comprehensive literature review was conducted to determine the maximum residual-gas saturation (S_{grm}). Numerous studies were reviewed to find a value that most accurately represents the target formation. One report (Holtz, 2005) established a correlation between porosity and S_{grm}. Another report (Hovorka, 2003), based on one of the first CCS pilots within the United States, used a relationship between porosity and S_{grm} similar to the first report. A chart illustrating the relationship between porosity and the maximum residual-gas saturation for unconsolidated Miocene sands is displayed in Figure 2-22 (Holtz, 2005). [redacted]

[redacted]

Figure 2-22 – Porosity vs. Residual Gas Saturation Relationship (Holtz, 2005)

Relative Permeability Curves

The absolute permeability of a porous medium is the permeability when only a single fluid is present within the pore space. When only one fluid is present within the reservoir, the effective permeability is equal to the absolute permeability. However, the effective permeability decreases as new fluids are introduced into the reservoir. This phenomenon is depicted by relative permeability curves, which illustrate the effective permeability of two or more fluids as they flow through a porous medium.

The GEM utilizes hysteresis modeling to establish the amount of supercritical CO_2 that is residually trapped. The hysteresis model enables the simulation of both drainage and imbibition processes. *Drainage* is the process of a nonwetting fluid (supercritical CO_2) displacing the wetting fluid (brine) as it is injected into and migrates through the reservoir. *Imbibition* refers to the reentry of the brine into the pore space, during which a certain amount of CO_2 becomes effectively trapped within the pore space.

In the absence of site-specific core data, relative permeability curves were constructed based on a literature review of similar depositional environments. The Corey-Brooks equations were used to generate the relative permeability curves used in the model. [redacted] iterature suggests that the K_{rw0} endpoint can be as high as 1.0 for analogous formations (Benson et al., 2013). [redacted]

[redacted]

[redacted] The data pertaining to the construction of the relative permeability curves are based on multiple references from the literature review (Bachu and Bennion, 2008; Bachu, 2012; Krevor et al., 2012). Subsequently, the imbibition curves were internally computed in GEM using the Carlson and Land method. Figure 2-23 shows the drainage and imbibition relative-permeability curves used in the model.

[redacted]

Figure 2-23 – Two-phase relative permeability curves implemented in the model.

[redacted] The model and subsequent curves will be updated after the cores have been tested and analyzed.

2.6 Well Operations Setup

For the Titan Project, the wellbore models for both wells were set up using the proposed wellbore schematics (WBS) along with assumptions provided in Table 2-4. Three primary constraints were imposed in GEM to limit the pressure response and CO_2 plume growth: (1) a maximum injection rate of [redacted] MMT/yr, (2) a maximum bottomhole pressure (BHP) gradient of [redacted] psi/ft, and (3) an injection period [redacted] years for both the Cronos No. 1 and Rhea No. 1 injection wells. Based on the proposed WBS, Titan plans to implement a [redacted] inch (in.) tubing string. This tubing size was considered when calculating the wellhead pressure (WHP) in GEM.

Table 2-4 – Well Hydraulics Input Summary

Inputs	Cronos No. 1 Values	Rhea No. 1 Values
Maximum Injection Rate (MMT/yr)	[redacted]	[redacted]
Pressure Constraint Gradient (psi/ft)	[redacted]	[redacted]
Injection Duration (yrs)	[redacted]	[redacted]
Tubing Inner Diameter (in.)	[redacted]	[redacted]
Tubing Setting Depth (ft)	[redacted]	[redacted]
Roughness Factor	[redacted]	[redacted]
Compressor Outlet Temperature (°F)	[redacted]	[redacted]
Compressor Outlet Pressure (psi)	[redacted]	[redacted]

Each injection well is divided into multiple completion stages to optimize the usage of available pore space. Each completion stage represents a portion of the reservoir that will be injected into at a given time. Figure 2-24 provides a theoretical depiction of the completion strategy planned for carbon sequestration. At each new completion, the pressure constraint is updated based on the upper perforation depth. This strategy is done to ensure that the BHP never exceeds the calculated fracture gradient. [redacted] A general description of the completion strategies is summarized in Tables 2-5 and 2-6.

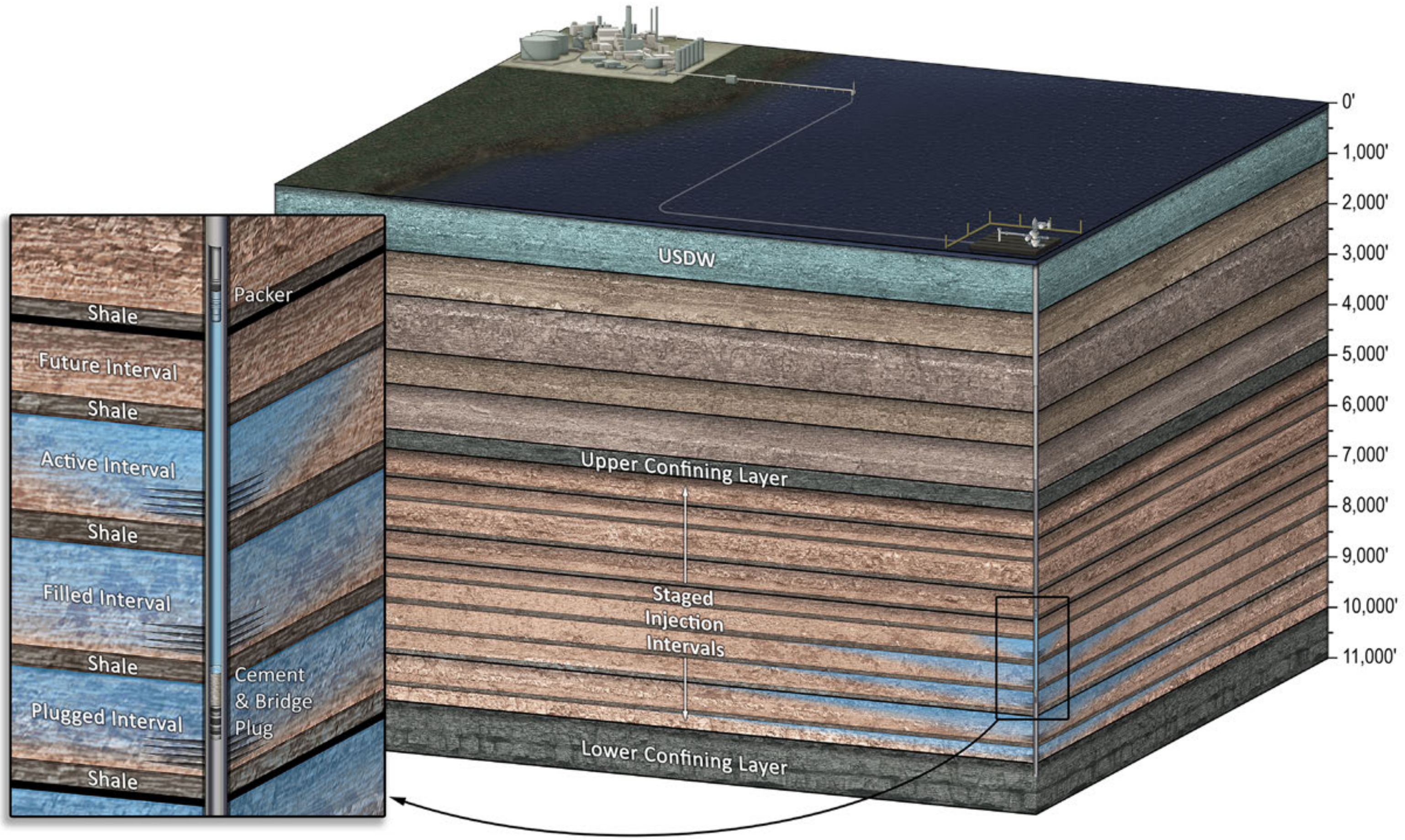

Figure 2-24 – Depiction of Completion Strategy

Table 2-5 – Summary of Completion Stages for Cronos No. 1

Stage	Top Perf (ft)	Bottom Perf (ft)	Gross Thickness (ft)	Net Pay (ft)	Duration (yrs)
[redacted]	[redacted]	[redacted]	[redacted]	[redacted]	[redacted]

Table 2-6 – Summary of Completion Stages for Rhea No. 1

Stage	Top Perf (ft)	Bottom Perf (ft)	Gross Thickness (ft)	Net Pay (ft)	Duration (yrs)
[redacted]	[redacted]	[redacted]	[redacted]	[redacted]	[redacted]

[redacted]

2.7 Model Results

2.7.1 Active Injection Operations of Proposed CO_2 Injector

During the life of the CO_2 injectors, the BHP and injection rate are simulated for each completion stage. Figures 2-25 and 2-26 depict the injection rates and BHP responses during operational activities. The rates are held at a constant rate of [redacted] MMT/yr for the injection periods for both wells, and the BHP never exceeds 90% of the fracture gradient. Because of the relative permeability, the BHP “spikes” at the start of each stage of injection. Once the CO_2 flow is established, the reservoir pressure declines to the expected values.

[redacted]

Figure 2-25 – Modeled BHP and Injection Rate for Cronos No. 1

[redacted]

Figure 2-26 – Modeled BHP and Injection Rate for Rhea No. 1

The WHP was calculated using GEM. Values such as tubing inner diameter, tubing setting depth, roughness factor, and compressor outlet pressure and temperature from Table 2-4 (*Section 2.6*) were used as inputs for the wellbore model. The calculations used BHP outputs from GEM to estimate the WHP.

Based on the model simulation, the maximum expected BHP of Cronos No. 1 is [redacted] psi during the life of the project, evaluated at [redacted]. On average, the BHP of the well will be [redacted] psi. The maximum WHP is calculated to be [redacted] psi with an average of [redacted] psi. Table 2-7 highlights the outputs for this injection well as modeled in GEM.

Table 2-7 – Cronos No. 1 Model Outputs

Stage	Year	Max Rate (MMT/yr)	Avg Rate (MMT/yr)	Max BHP (psi)	Avg BHP (psi)	Max WHP (psi)	Avg WHP (psi)
[redacted]							

Based on model simulation, the maximum expected BHP of Rhea No. 1 is [redacted] psi during the life of the Titan Project, evaluated at [redacted] ft. On average, the BHP of the well will be [redacted] psi. The maximum WHP is calculated to be [redacted] psi with an average of [redacted] psi. Table 2-8 provides the outputs for this injection well as modeled in GEM.

Table 2-8 – Rhea No. 1 Model Outputs

Stage	Year	Max Rate (MMT/yr)	Avg Rate (MMT/yr)	Max BHP (psi)	Avg BHP (psi)	Max WHP (psi)	Avg WHP (psi)
[redacted]							

Reservoir pressure is expected to increase from initial conditions during the active injection period. The highest increase is expected at the wellbore and then propagates throughout the formation rock, resulting in a general increase of pressure within the aquifer region. This pressure-increase phenomenon is referred to as “pressure buildup,” which is monitored by the rise of reservoir pressure as well as its associated gradient based on the top of the perforated interval.

Figures 2-27 and 2-28 represent the maximum pressure buildup at the two injection wells—the BHP result—which represents the maximum pressure seen within the reservoir at any given time. In addition, since these pressure values are retrieved at different depths, the pressure gradient is also calculated as pressure divided by depth (i.e., the calculated pressure gradient). [redacted] As shown in Figures 2-27 and 2-28, the pressure gradient never exceeds the constraint (90% of FG) imposed on the wells, to allow for the safe injection of supercritical CO_2.

[redacted]

Figure 2-27 – Pressure Buildup for Cronos No. 1 During Active Injection Operations

[redacted]

Figure 2-28 – Pressure Buildup for Rhea No. 1 During Active Injection Operations

The elevated pressure in the saline aquifer quickly dissipates once active injection operations cease. [redacted] Figures 2-29 and 2-30, for the two wells respectively, show the pressure buildup throughout the life of the project.

[redacted]

Figure 2-29 – Pressure Buildup for the Life of Cronos No. 1

[redacted]

Figure 2-30 – Pressure Buildup for the Life of Rhea No. 1

2.8 CO_2 Plume Migration for AOR Delineation

According to TAC **§5.203(d)** [40 CFR **§146.84**], the AOR must be determined by the maximum extent of either the supercritical CO_2 plume or critical pressure front—or both. The first review starts with the extent of the CO_2 plume. The Occupational Safety and Health Administration (OSHA) has set an acceptable exposure limit of CO_2, indicating that up to 30,000 ppm over a 10-minute period is within safe guidelines. [redacted] Both Titan injection wells were used to determine the plume extent. Injection of CO_2 into the two wells results in a combined supercritical CO_2 plume.

Due to the geologic structure of the reservoir and presence of channels, the CO_2 plume may migrate in different directions from the injector wells. Channels may act as a high permeability conduit that CO_2 can migrate further through. Structural dip also influences the migration of the CO_2 plume. The less dense CO_2 migrates upward due to buoyancy effects until it reaches an impermeable layer, like an interbedded shale. The formation's upward dip then facilitates migration. [redacted] Figure 2-31 provides a 3D view of the stabilized plume in the year [redacted] highlighting the different directions in which the plume migrates, while also illustrating the concept of structural trapping. Interbedded shales and shale baffles serve as traps for the supercritical CO_2 to prevent further upward and lateral migration. The largest extent of the plume is determined by the maximum saturation experienced in all the modeled layers at a specified point in time.

[redacted]

Figure 2-31 – A vertical 3D representation (left) and aerial view (right) of supercritical CO_2 plume in [redacted] colored by CO_2 saturation.

The CO_2 plume [redacted] for both injection wells. Figures 2-32 through 2-35 show the cross-sectional view of the plumes and highlight how the shape and size of the plumes vary in each sand package. Between each sand package, interbedded clay-rich shales exist that help structurally trap CO_2 and inhibit vertical migration. The current completion strategy is designed to use these interbedded shales, to help permanently sequester CO_2 between completion stages while minimizing the plume footprint.

[redacted]

Figure 2-32 – West-east cross-sectional view at Cronos No. 1 [redacted] colored by CO_2 saturation.

[redacted]

Figure 2-33 – West-east cross-sectional view at Rhea No. 1 [redacted], colored by CO_2 saturation.

[redacted]

Figure 2-34 – South-north cross-sectional view at Cronos No. 1 [redacted], colored by CO_2 saturation.

[redacted]

Figure 2-35 – South-north cross-sectional view at Rhea No. 1 [redacted] colored by CO_2 saturation.

The CO_2 plume in Figure 2-36 is delineated from the maximum CO_2 saturation seen in each layer of the model. The plume extent is taken in [redacted]

[redacted]

Figure 2-36 – Aerial View of Supercritical CO_2 Front [redacted] Outlined in Black

2.8.1 Trapping Summary

Figure 2-37 shows the breakdown of the trapping mechanism. Once injection stops [redacted] the mobile CO_2 quickly decreases as supercritical phase CO_2 migrates through pore space and is trapped. Over the life of the project, [redacted] These percentages of trapped CO_2 agree with data from literature based on the maximum residual gas saturation value implemented in the model (Metz et al. 2005; Holtz 2002).

[redacted]

Figure 2-37 – Modeled Trapping Mechanisms (the red line designating end of injection)

2.8.1.1 Stabilized Plume

Plume stabilization occurs when the rate of growth or positional change has slowed to a nearly imperceptible change per year. At that point, the CO_2 plume is considered hydrodynamically trapped in the pore space. This stabilization point is determined by the model output, where the areal growth rate is [redacted]

The reservoir model determines that plume stabilization occurs by the [redacted] To be conservative and in accordance with [40 CFR **§146.93(b)(1)**], the plume is monitored for 50 years after injection ceases, even though stabilization has occurred. Because of the proximity of the two injection wells, the plumes of both coincide with one another to create one plume. The plume growth therefore considers the one combined plume. While incidental plume movement may occur after this period, the reservoir model indicates that the plume will continue to remain on acreage that Titan has secured by underground storage easements. Figure 2-38 demonstrates that the rate of plume movement decreases to [redacted] post-injection.

[redacted]

Figure 2-38 – Plume Growth Over Time

2.9 Critical Pressure Front for AOR Delineation

In accordance with TAC **§5.203(d)** [40 CFR **§146.84**], the AOR was delineated by the critical pressure front created by the injection of supercritical CO_2 into a saline aquifer. Critical pressure is the increase in reservoir pressure that may push in situ fluids out of the injection zone and into the lowermost USDW, in the presence of a bridging conduit such as an unplugged borehole. The first step to predict the pressure front is to calculate the critical pressure for each completion stage. Once critical pressure is determined, a numerical simulation is used to predict the size and shape of the critical pressure front. A conservative approach on determining the critical pressure front was used [redacted]

[redacted] This case allows for a larger and therefore more conservative strategy of calculating the critical pressure front.

The EPA has outlined three potential methodologies to calculate the critical pressure. Method 2, which uses Nicot's method to calculate the critical pressure, was used in this model. Nicot assumes that the reservoir is in hydrostatic equilibrium, neither under- nor overpressurized, and that a direct path between the two zones exists. This path could be in a hypothetical incorrectly plugged-and-abandoned wellbore or some other subsurface feature.

For the purpose of the critical pressure calculations, the base of the USDW was estimated to be at [redacted] true vertical depth (TVD), as stated in *Section 1.8*. This depth is based on analysis of offset wells nearest to the proposed injector locations [redacted] that indicate the depth of the USDW's base within plugging and abandonment reports of [redacted] TVD. Said plugging and abandonment reports are in alignment with the Bureau of Economic Geology (BEG) estimations for the area, as stated in *Section 1.8.4*. The USDW base will be confirmed by the Groundwater Advisory Unit of the Texas Railroad Commission (TRRC). The critical pressure was calculated for each completion of each injection well, with the top of injection [redacted] The fluid in the injection zone is assumed to be brine, with [redacted] TDS, which results in a [redacted] psi/ft pressure gradient. The fluid within the USDW was assumed to be fresh water (less than 10,000 ppm), with a pressure gradient of 0.436 psi/ft. The inputs used in the calculation are provided in Table 2-9.

Table 2-9 – Critical Pressure Calculation Parameters

Parameter	Symbol	Value
Depth to Base of USDW	(D_u)	[redacted]
Depth to Top of Injection Zone	(D_i)	[redacted]
Gradient of USDW	(G_u)	[redacted]
Gradient of Injection Zone	(G_i)	[redacted]

The coefficient (ξ) is first calculated in Equation 4 using the pressure gradients and depths for the base of the USDW and top of the injection zone.

(Eq. 4)

$$\xi = \frac{G_i - G_u}{D_i - D_u}$$

[redacted]

The critical pressure rise (ΔP_c) is then calculated using Equation 5. The inputs include the coefficient (ξ) calculated in Equation 4 and the depths for the base of the USDW (D_u) and top of the injection zone (D_i).

(Eq. 5) $$\Delta P_c = \frac{1}{2} * \xi * (D_i - D_u)^2$$

[redacted]

The resulting critical pressure rise for the uppermost stage is positive, indicating that the reservoir pressure may be safely increased by approximately [redacted] psi, without risk of fluid migration to the USDW. The calculated critical pressure rise for each of the completion stages for both injection wells is included in Tables 2-10 and 2-11.

Table 2-10 – Cronos No. 1 Critical Threshold Pressure for Each Completion Stage

Completion Stage	Depth to Top of Injection Zone (ft)	Critical Threshold Pressure (psi)
[redacted]	[redacted]	[redacted]

Table 2-11 – Rhea No. 1 Critical Threshold Pressure for Each Completion Stage

Completion Stage	Depth to Top of Injection Zone (ft)	Critical Threshold Pressure (psi)
[redacted]	[redacted]	[redacted]

Due to the complex and heterogeneous nature of the reservoir, the critical pressure front may propagate in different directions. The critical pressure front is delineated by the maximum extent of the pressure front from each completion stage. [redacted]

[redacted]

The AOR is, in part, determined by the [redacted] 1. Figure 2-39 provides a snapshot of the largest extent of the critical pressure front experienced in the model.

[redacted]

Figure 2-39 – Greatest Extent of Critical Pressure Front, Outlined in Pink

2.10 Final AOR

The maximum CO_2 plume and critical pressure front delineate the AOR, which determines the necessary evaluation of, and potential corrective action needed for, any offset wells. The CO_2 saturation front is determined by the greatest extent of the fluid in any direction throughout the injection zone. The acceptable exposure limit of CO_2 set by OSHA indicates that up to 30,000 ppm over a 10-minute period is within safe guidelines [redacted]. The critical pressure front was determined from the greatest areal extent of all completion stages for both injection wells. Figure 2-40 provides the final AOR outlines for the project.

[redacted]

Figure 2-40 – Cronos No. 1 and Rhea No. 1 (Titan Project) Final AOR

2.11 References

Bachu, S. (2012). Drainage and Imbibition CO2/Brine Relative Permeability Curves at In Situ Conditions for Sandstone Formations in Western Canada. *Energy Procedia* 37. 10.1016/j.egypro.2013.07.1

Bachu, S., and Bennion, B. (2008). Effects of in-situ conditions on relative permeability characteristics of CO2-brine systems. *Environ Geol* 54: 1707–1722.

Backeberg, N., Iacoviello, F., Rittner, M. et al. (2017). Quantifying the anisotropy and tortuosity of permeable pathways in clay-rich mudstones using models based on X-ray tomography. *Scientific Reports*, 7. 10.1038/s41598-017-14810-1.

Benson, S., Pini, R., Reynolds, C., and Krevor, S. (2013). Relative Permeability Analysis to Describe Multi-Phase Flow in CO2 Storage Reservoirs; No. 2; Global CCS Institute: Melbourne, Australia.

Burnside, N. M., and Naylor, M. (2014). Review and implications of relative permeability of CO2/brine systems and residual trapping of CO2, *International Journal of Greenhouse Gas Control*, Volume 23.

Chen, X., Gao, S., Kianinejad, A., and DiCarlo, D. A. (2017). Steady-state supercritical CO2 and brine relative permeability in Berea sandstone at different temperature and pressure conditions. *Water Resources Res.* 53: 6312– 6321. https://doi:10.12/2017WR020810.

Chudi, O. K., Lewis, H., Stow, D. A. V., and Buckman, J. O. (2016). Reservoir quality prediction of deep-water Oligocene sandstones from the west Niger Delta by integrated petrological, 61petrophysical and basin modelling. In: Armitage, P.J., Butcher, A. et al., ed., Reservoir Quality of Clastic and Carbonate Rocks: Analysis, Modelling and Prediction. Geological Society, London, Special Publications, 435. https://doi.org/10.1144/ SP435.8.

Eaton, B. A. (1969). Fracture Gradient Prediction and Its Application in Oil Field Operations. *Journal of Petroleum Technology*, 25-32.

Holtz, M. H. (2002). "Residual Gas Saturation to Aquifer Influx: A Calculation Method for 3-D Computer Reservoir Model Construction." Paper presented at the SPE Gas Technology Symposium, Calgary, Alberta, Canada, April 2002. https://doi.org/10.2118/75502-MS.

Holtz, M. H. (2005). "Reservoir Characterization Applying Residual Gas Saturation Modeling, Example From the Starfak t1 Reservoir, Middle Miocene Gulf of Mexico."

Hovorka, S. D., Holtz, M. H., Sakurai, S. et al. (2003). Frio pilot in CO2 sequestration in brine-bearing sandstones: The University of Texas at Austin, Bureau of Economic Geology, report to the Texas Commission on Environmental Quality to accompany a Class V application for an experimental technology pilot injection well. *GCCC Digital Publication Series No. 03-04*.

Krevor, S. C. M., Pini, R., Zuo, L., and Benson, S. M. (2012). Relative permeability and trapping of CO2 and water in sandstone rocks at reservoir conditions. *Water Resources Res.*

McCain, W. D. (1991). Reservoir-Fluid Property Correlations—State of the Art. *SPE Res Eng* 6: 266–272. https://doi.org/10.2118/18571-PA.

Metz, B., Davidson, O., de Connick, H., Loos, M., and Meyer, L. ed. (2005). IPCC Special Report on Carbon Dioxide Capture and Storage. Cambridge, United Kingdom: Cambridge University Press.

Molina, O., Vilarrasa, V., and Zeidouni, M. (2017). Geologic Carbon Storage for Shale Gas Recovery. *Energy Procedia* 114: 5748-5760. 10.1016/j.egypro.2017.03.1713.

Müller, N. (2011). Supercritical CO2-Brine Relative Permeability Experiments in Reservoir Rocks—Literature Review and Recommendations. *Transp Porous Med* 87: 367–383.

Newman, G. H. (1973). Pore-volume compressibility of consolidated, friable, and unconsolidated reservoir rocks under hydrostatic loading. *Journal of Petroleum Technology* 25(02): 129–134. https://doi.org/10.2118/3835-pa.

Sun, J., Deng, J., Yu, B., and Peng, C. (2015). Model for fracture initiation and propagation pressure calculation in poorly consolidated sandstone during waterflooding. *Journal of Natural Gas Science and Engineering* 22: 279-291. 10.1016/j.jngse.2014.12.004

Taylor, T. R., Kittridge, M. G., Winefield, P. et al. (2015). Reservoir quality and rock properties modeling – Triassic and Jurassic sandstones, greater Shearwater area, UK Central North Sea. *Marine and Petroleum Geology* 65: 1–21. https://doi.org/10.1016/j.marpetgeo.2015.03.020.

Weber, K., and van Geuns, L. (1990). Framework for Constructing Clastic Reservoir Simulation Models. *Journal of Petroleum Technology*, 1248-1253, 1296-1297.